Yifeng Gong[1]
Department of Mechanical Engineering,
Case Western Reserve University,
Cleveland, OH 44106
e-mail: yxg553@case.edu

Alexander M. Behr
Department of Computer and Data Sciences,
Case Western Reserve University,
Cleveland, OH 44106
e-mail: amb296@case.edu

Nicole M. Graf
Department of Mechanical Engineering,
Case Western Reserve University,
Cleveland, OH 44106
e-mail: nmg63@case.edu

Kaiyi Chen
Department of Electric Engineering,
Case Western Reserve University,
Cleveland, OH 44106
e-mail: kxc581@case.edu

Zhili Gong
Department of Mechanical Engineering,
Case Western Reserve University,
Cleveland, OH 44106
e-mail: zxg204@case.edu

Kathryn A. Daltorio
Assistant Professor
Department of Mechanical Engineering,
Case Western Reserve University,
Cleveland, OH 44106
e-mail: kam37@case.edu

A Walking Claw for Tethered Object Retrieval

Mobility and manipulation are often considered separately, with independent degrees-of-freedom (DOF) for each. However, here we show that using the legs for both walking and grasping increases the versatility of both tasks. Our robot has four DOF: drive and lift for left and right pairs of legs. The legs use a reduced actuation Klann mechanism. The lift DOF rotates the entire trajectory of the legs, which enables gait modulation, climbing, and grasping. This demonstrates the feasibility of a novel operational concept: a robot that can approach, climb onto, and securely grasp an object that can then be lifted via a load-bearing tether. Specifically, we show the kinematics to enable small robots to climb onto rectangular objects up to 67% robot height and grasp objects between 43% and 72% of the robot's length. With these kinematics, a robot can be scaled for specific terrains and object sizes, with potential application in construction, search and rescue, and object retrieval. [DOI: 10.1115/1.4055812]

Keywords: grasping and fixturing, legged robots, mechanism design, mobile robots, robot design

1 Introduction

Mobile robots can access otherwise inaccessible places, and adding manipulation enables utility beyond inspection and surveillance. In factory settings, mobile robots can lift and position inventory by taking advantage of standard-sized pallets. However, in terrain environments that are sufficiently uneven as to require legs, the grasping tasks are likely to be similarly unstructured. Here, in order to grasp objects in natural terrain, we propose an underactuated robot in which the same legs are used for both locomotion and grasping, as shown in Fig. 1.

The operational concept of such a robot is shown in Fig. 1. First, the robot takes advantage of the walking ability of its legs for controlled walking over potentially uneven terrain. Second, when the robot finds a target object to grasp, the robot places its legs on top of an object (we refer to this in the paper as a "half climb"). Third, the robot climbs on top of it until the front and back legs are placed on the opposite sides of the object ("full climb") so that the legs can be pressed against the obstacle sides with a secure grasp. Fourth, a load-bearing tether can provide the main lift force to retrieve the target object. In this way, a robot can be suspended from a crane, boat, rotorcraft, or a larger robot to retrieve samples, essential tools, or hazardous materials. While many mobile robots use legs for rough terrain [1–5] and force closure with claw-like graspers [6–9], to our knowledge, there is no other robot using the same legs for both tasks.

While power autonomy is an important goal for some small robots, here having a tether can be valuable. Search and rescue teams prefer tethered robots [10] because the robot can always be retracted. A robot that is small enough to explore confined spaces and can be dragged back with a larger object in tow could be especially helpful for clearing blocked infrastructure or search and rescue. Alternatively, a self-positioning end effector for a

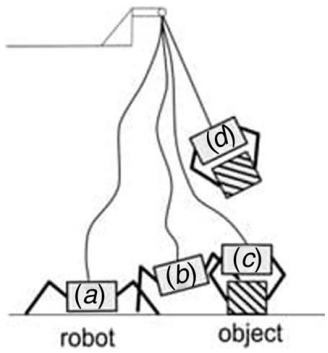

Fig. 1 The proposed tethered robot will (*a*) walk to the object, (*b*) climb the object, (c) grasp the object, and (*d*) be pulled by the tether while grasping the object

[1]Corresponding author.

Contributed by Mechanisms and Robotics Committee of ASME for publication in the Journal of Mechanisms and Robotics. Manuscript received March 14, 2022; final manuscript received September 2, 2022; published online December 9, 2022. Assoc. Editor: Hao Su.

crane hook would save humans the role of securing loads in difficult-to-access spots. For example, marine robots to walk along the sea floor and retrieve environmental samples, hazards such as unexploded munitions, or rare metal nodules [11] have the potential to be both profitable and environmentally friendly. Currently, flying robots have to precisely align a hook or connector to a load, which requires a combination of skill and appropriate weather conditions [12]. A walking and grasping robot would reduce required precision and enable access to objects that are occluded from the sky by overhanging structures or plants.

Typically, in mobile robots with manipulation arms, the grasped object is small relative to the robot. One reason for this is that if a separate manipulation appendage is to be used, special care must be taken so that the manipulation does not destabilize the robot. Thus, manipulation tasks that seem simple to humans are challenges for bipedal robots [13]. For example, if a humanoid robot bends too far at the waist to reach an object, the weight of the torso and arms can move the center of mass (CoM) outside its support polygon, causing the robot to fall over. Adding more legs makes it possible to access environments that are typically more difficult for bipedal robots to traverse, while maintaining the ability to interact with the environment, such as opening doors with an arm appendage.[2] Having more legs will improve the stability, however, it is still hard for quadruped and hexapods robots to grasp objects of similar size by using a separate manipulator.[3] Unlike many heavy-legged robots manipulating small objects, in suspended retrieval applications, the grasping robot needs to be small and light relative to the payload because this reduces load requirements for the crane or robot. Here, our approach is different from most legged robots which can grasp objects in their environment by an attached robotic gripper [14–18] in that the whole robot is intended to grasp the object. Rather than reserve some legs for locomotion, this enables more legs to contribute to the secure form or force closure [19] of the grip. This concept builds on our earlier work in climbing robots in which we argue that using the legs for distributed inward gripping enables robots to walk on surfaces regardless of the relative orientation of gravity [20]. Unlike climbing robots, which often require specialized end effectors [21], here the same tapered legs that are key for secure walking in sand and rocks [22] will be used like the fingers of a grasper.

Successfully retrieving objects must always consist of two parts, first positioning end effectors to make contact, and second applying required forces at the contact points. For the second part, these required forces are a direct function of the object weight, the friction coefficient, and the match between surfaces [23]. For example, soft contacts in which the grasper surface can conform to match the object surface profile will provide the most secure grasps [24]. For rigid objects, the mapping between forces applied and required torque is a straightforward mechanics problem, with closed loop force control enabling maintenance of the grasp. As robots become more dexterous, the first part, positioning end effectors in various ways, has received more attention. Different human-like grasps can be selected [25] and objects can be manipulated within the hand by moving contact surfaces or using multiple grips [26]. Most of this literature has naturally focused on gripping from a robotic arm, usually on a fixed base [27], and sometimes on a mobile platform [28]. Here, we focus on positioning end effectors (in this case foot instead of fingers) for grasping with the legs rather than the arms of a mobile robot.

Determining the minimum number of degrees-of-freedom (DOF) is essential for these applications. Fewer DOF makes robots easier to control (and therefore more widely usable in emergencies such as search and rescue). Reduced actuation [29] can also make the robot lighter, and thus potentially deployable from the air. As is typical for mobile robots, we expect that using a single drive motor rather than multiple independent actuators for each leg increases performance by reducing required the torque-to-weight ratio and decreases the cost for robustness because actuators are often the most costly component of a robot. Reduced actuation legs that convert continuous rotation to a walking trajectory have taken many forms. RHex legs are a spoke with variable speed in stance and swing [30]. Wheel-legs have more spokes and typically operate at a constant speed [29]. Other types of four-bar mechanisms are possible [31]. Jansen linkages have 11 links [32,33], but Klann linkages have only seven links which make them a more common choice [34–38]. This Klann linkage is designed to transfer the rotating motion from the motor into a periodic trajectory containing swing and stance phases with only one DOF. It saves the simplicity of the mechanical structure, however, only one gait is produced with one specific design. By changing the linkage, gaits can be adapted to applications, such as walking on specific terrain or digging the ground [35]. Compliance can also be added to the Klann mechanism to better overcome the obstacles [34]. However, all Klann robots we know only aim at walking and moving across obstacles, which are never developed in other fields such as grippers.

To our knowledge, this paper is the first time in which Klann mechanism legs have been added to the end of a coxa joint. Body joints have been studied for flexibility in cheetah-like running [39] and climbing [40]. For example, adding a body joint to a robot with simple wheel-legs enables a robot to climb stairs [41] and make climbing transitions from one surface to another [42]. Other body joints have been combined with four-bar mechanisms for climbing [43]. Other legged robots can climb by taking advantage of many independently controlled joints each with a wide range of joint motions [44]. Here, the linkage design separates the functions of the DOF when the Klann mechanisms are driven the robot moves forward (drive DOF) whereas when the coxa is driven the legs pull inward or outward like a claw (lift DOF), see Fig. 2.

The intended contribution of this paper is to demonstrate that a four DOF legged robot can both walk over and grasp objects. An articulated coxa joint was added to a reduced actuated Klann leg. The extra DOF more than triples the climbable obstacle height and enables grasping of a range of rectangular object widths. In future work, the robot can be adapted and customized for other environments and object shapes, and foot sensors as in Ref. [45] could be added to automate object recognition and grasping.

2 Mechanism Design

The goal is to design compatible DOF for both drive and lift. The drive DOF is responsible for creating a periodic gait trajectory, using continuous rotation as input for efficiency and simplicity.

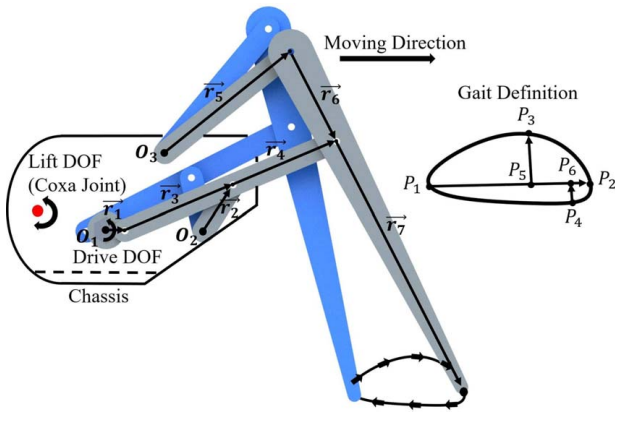

Fig. 2 Dual Klann leg: Drive DOF to produce gait, lift DOF to lift legs up and down, length of seven Klann links (from r_1 to r_7), the position of three fixed rotation joints (O_1, O_2, O_3), the position of the coxa joint and the gait. Optimized Klann gait: Liftoff point P_1, touchdown point P_2, stride length $P_1P_2 = 47.9$ mm, swing height $P_3P_5 = 14.8$ mm, and stance variation $P_4P_6 = 5.4$ mm.

[2] https://www.youtube.com/watch?v=6Zbhvaac68Y
[3] See Note 2.

The lift DOF is responsible for raising the legs to climb onto the obstacle and for pulling the legs inward to grasp the obstacle once it has been climbed. Since the left and right halves of the robot need to lift onto the obstacle sequentially, the robot needs two lift DOF (left and right). In order to steer into position, the robot also needs two drive DOF, for a total of four DOF. Thus, the Klann robot can be considered a differential drive model. The two legs' speed on both side is the same by using one control signal. Synchronization between these two legs makes the control system more complex and not helpful in movement.

2.1 Leg Mechanisms. A dual Klann leg was used to improve the static stability and smoothness with reduced DOF. A 50% duty cycle (half of the legs are in the stance phase and half are in the swing) works well for Klann foot trajectories at a constant drive speed. Thus, each leg pair is driven together at a 180° offset to form the dual Klann legs (Fig. 2). At least six legs or three dual Klann legs are needed for an alternating tripod gait. However for left-right and front-back symmetries, four dual legs are required. The additional legs help distribute weight and prevent the robot from sinking into substrates. In addition, a support triangle can be maintained even with a lifted leg. The same signal is used to control the DC motors on both side of the robot, which allows the four dual legs to have two drive DOF for forward and backward walking and turning. The drive DOF rotates crank r_1 about the drive motor O_1 resulting in a cyclic leg trajectory that will include both stance and swing. Through the link lengths from r_1 to r_7 and the position of the rotational joints O_1, O_2, O_3, the position vector of the end effector $\mathbf{r}$ can be determined from Eq. (1). The generated gait is "the locked gait" where the coxa angle is fixed at 0°.

$$\mathbf{r} = \mathbf{r_1} + \mathbf{r_3} + \mathbf{r_4} + \mathbf{r_7} \tag{1}$$

2.2 Gait Optimization. For the closed-chain leg mechanism, the design goal of its generated single gait is to walk smoothly and swing across small obstacles like pebbles on uneven terrains [46,47]. Here, we will first optimize the gait shape with the Klann mechanism for efficient walking. The definition of the gait shape is shown in Fig. 2. P_1 and P_2 are the liftoff point and the touchdown point with phase difference π, which divide the swing phase and the stance phase. In one single trajectory, the gait parameters should satisfy the following requirements: (a) stride length P_1P_2 should be as horizontal as possible so that both stance phases of front and back legs would be co-linear. (P_1P_{2x} must be large, while P_1P_{2y} should be small), (b) stride length P_1P_2 should be large enough to achieve fast speed, (c) swing height P_3P_5 should be as long as possible to swing across obstacles, and (d) stance variation P_4P_6 should be relatively small to reduce moving vibration. The objective function is shown in Eq. (1), where coefficients are chosen as $a=-1$, $b=100$, $c=-10$, and $d=20$. The optimization is performed to realize all requirements, however, every variable would contribute to the gait shape. If the gait parameter is desired to be large, its coefficient needs to be negative so that the objective function can find the optimized point by reaching the global or local minimum and vice versa. Additionally, if the gait parameter is inherently smaller than others like P_1P_{2y}, the absolute value of the coefficient should be large. Otherwise, the gait parameter will not be optimized, because it doesn't contribute to the objective function. There is a tradeoff between stride length, swing height, and the stance variation, which means it is impossible to fix one characteristic and then enlarge another. Moreover, only links are optimized, since the position of three rotational joints (O_1, O_2, and O_3) would easily convert the gait to an unfavorable shape. Specifications of the optimized links are shown in Table 1.

$$f = a * P_1P_{2x}^2 + b * P_1P_{2y}^2 + c * P_3P_5{}^2 + b * P_4P_6{}^2 \tag{2}$$

By using the sequential quadratic program, the optimized gait and gait parameters are generated: $P_1P_2 = 47.9$ mm, $P_3P_5 = 14.8$ mm, $P_4P_6 = 5.4$ mm, $\arctan((P_1P_2)_y/(P_1P_2)_x) = 0$. Because the stance straightness is $P_4P_6/P_1P_2 = 11.3\%$ and the stance variation is only 5.4 mm, P_1P_2 is the approximate stance phase in the following kinematic analysis. In other words, the trajectory under P_1P_2 would be neglected.

Table 1 Specifications of the articulated Klann robot

Specifications	Value	Specifications	Value
Articulated Klann		**Lengths of links**	
Length	418 mm	r_1	8.2 mm
Width	398 mm	r_2	24.0 mm
Height	178 mm	r_3	51.5 mm
Total mass	2.03 kg	r_4	49.2 mm
Mass of one dual leg	0.28 kg	r_5	70.8 mm
Number of dual legs	4	r_6	44.2 mm
Pololu 3203 torque	7.4 kg · cm	r_7	123.8 mm
Pololu 4748 torque	4.9 kg · cm		

2.3 Coxa Joint Mechanism. There are many challenges to successfully grasp a specific object when operating in various terrains. While the dual Klann leg traditionally has a high level of stability, it is unable to overcome tall obstacles without the lift DOF. Furthermore, for grasping, the coxa joint should be adjustable and powerful to apply sufficient normal forces such that friction between the object and the dactyls will be enough to secure the desired payload. The two lift DOF were added to the two coxa joints on the end of the front legs. This improves the climbing ability as well as converts the walking machine to be an active gripper. Motors for lift DOFs are placed in the central chassis for design compactness, transmitting power to coxa joints through gearboxes. There are three main functions of coxa joints dealing with object retrieval: the front legs can step on a higher platform, the body chassis can be raised higher when all four legs are on the ground, and the robot can grasp a wider range of objects. The mechanical structure of the articulated Klann robot is shown in Fig. 3.

3 Kinematics

3.1 Klann Linkage Kinematics. To show the value of the coxa joint, we will compare the kinematics of the robot when the coxa is "locked" (i.e., the coxa fixed at 0°) with the workspace available when the coxa is active. When the coxa is active, the lift DOF

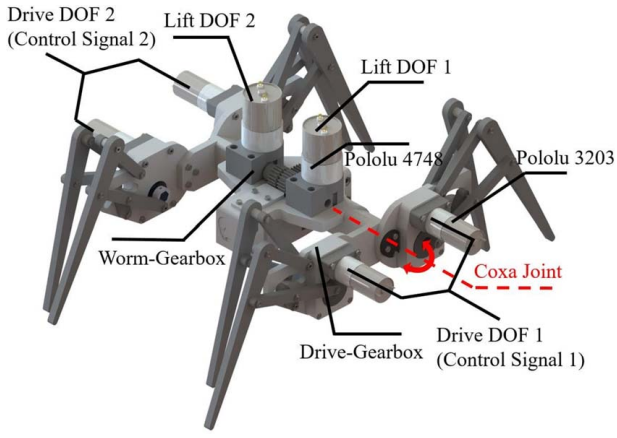

Fig. 3 Articulated Klann robot: Two drive DOF consist of four Pololu 3203 DC motors and four drive-gearboxes, where two motors on the same side are bound together for control. Two lift DOF consist of two Pololu 4748 DC motors and two worm gearboxes.

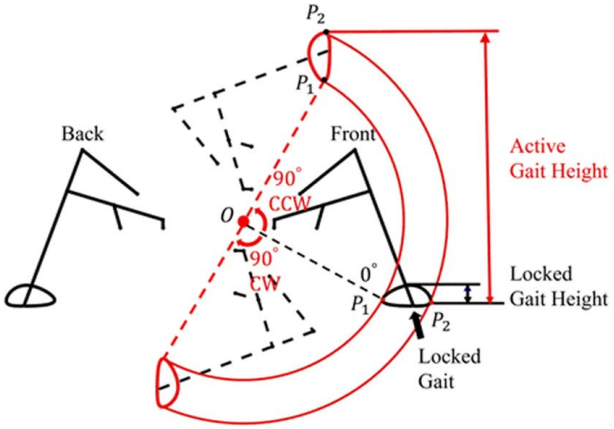

Fig. 4 The active Klann gait (lift DOF) is traced in red, with example stride lengths throughout the range of possibilities. The locked gait, shown in black, is the only possible gait for the robot when it is in its locked position (drive DOF). The locked robot has a limited locked gait height (14.8 mm). When the lift DOF enables the front legs to step on higher objects, active gait height (280 mm) is produced. *O* represents the coxa joint.

rotate the dual Klann legs about the coxa joint from 90° clockwise to 90° counterclockwise. This motion results in a larger workspace, as shown in Fig. 4, when using an active gait to find favorable climbing steps, not unlike the way our prior work uses body joints [48].

In addition to expanding the workspace, the coxa also rotates the Klann trajectory which affects walking behavior. When the stance phase (P_1P_2) of the trajectory is at a different angle for the front and rear legs, we can expect adaptive gaits for different environments that affect speed, moving direction, and potentially cause mechanical vibrations. At the locked position, the stance phases are co-linear for front and back legs which we originally assumed would be best for stability and speed when walking on flat ground. On other terrains, being able to create an inward trajectory might help the robot "grasp the ground" [22]. Therefore, we tested the robot at various coxa angles on various terrains.

3.2 Kinematic Predictions. In order to demonstrate that this design obeys expected kinematics, we analyze the kinematics. This analysis can also be inverted to scale a robot to grasp objects of the desired size.

For the climbing and grasping task of Fig. 7, there are three main kinematic requirements. First, the robot has to be able to put its legs on top of the obstacle, we refer to this as a "half climb" (Figs. 7(*a*)–7(*d*)). Second, the robot needs to be able to lift the body high enough to clear the top of the obstacle so that it can walk the legs across the obstacle. This is achieving a "full climb" (Figs. 7(*e*)–7(*f*)). Finally, the distance between end effectors needs to be adjusted to match the object, achieving a sufficient "grasp" so that the tether can pull the object from the ground (Figs. 7(*f*)–7(*g*)).

3.2.1 Half Body Climb. The maximum height of half climb depends on gait height. The locked robot has a gait height P_3P_5 of 14.8 mm. To stand on a higher platform, the first coxa joint lifts the first dual Klann leg up, while the other three end effectors stand on the ground, maintaining a support polygon. The active gait height is the height of P_2 with respect to the locked stance phase. Compared to the locked gait height, the active gait height is up to 280 mm when the coxa joint rotates 90° counterclockwise, as shown in Fig. 4. After the first leg is placed on the object, the second front dual leg will lift to be placed on the obstacle. The initial position will be oblique to the front face of the object, and during climbing, the robot can be maneuvered into a better position for lifting using the drive DOF.

3.2.2 Full Body Climb. A full climb is completed when the robot walks across the object until the front and back legs are on the opposite side of the object. If the front legs can reach the top, but then the central body cannot clear the top of the obstacle from the ground, the robot will be able to make a half climb but not a full climb. To successfully full climb, the whole chassis should be higher than the object. Therefore, the ability to clear the top is geometrically determined by the lowest point of the chassis (the lowest point is referred to as the body height H). No matter how many unnecessary parts of the body chassis can be eliminated to heighten the body, at least Klann linkage points need to be retained for the mechanical design. Thus, the basic Klann linkage analysis can tell us the best full climb ability, assuming the chassis does not have extra material on the bottom to interfere.

From the geometry, the rotation joint O_2 on the back linkage is considered as the lowest point of the central body to clear the top when the coxa joint rotates clockwise (CW) (coxa angle is referred to as α). The locked and active full body height ($\alpha = 40°$) are shown in Fig. 5. The body height (H) is changed by both the coxa angle CW (α) and the obstacle height (h), since the coxa joint can push the front legs inward to heighten the body, and the obstacle itself can raise the robot when the front legs step on it. The body height is expressed as Eq. (3). L_1, L_2 L_4, L_5 are fixed distance between points, whereas L_3 is changed when the coxa joint rotates. Thus, θ_1 is fixed based on the cosine law, and θ_2 and θ_3 can be expressed as $\theta_2 = f_1(\alpha)$ and $\theta_2 = f_2(\alpha, h)$.

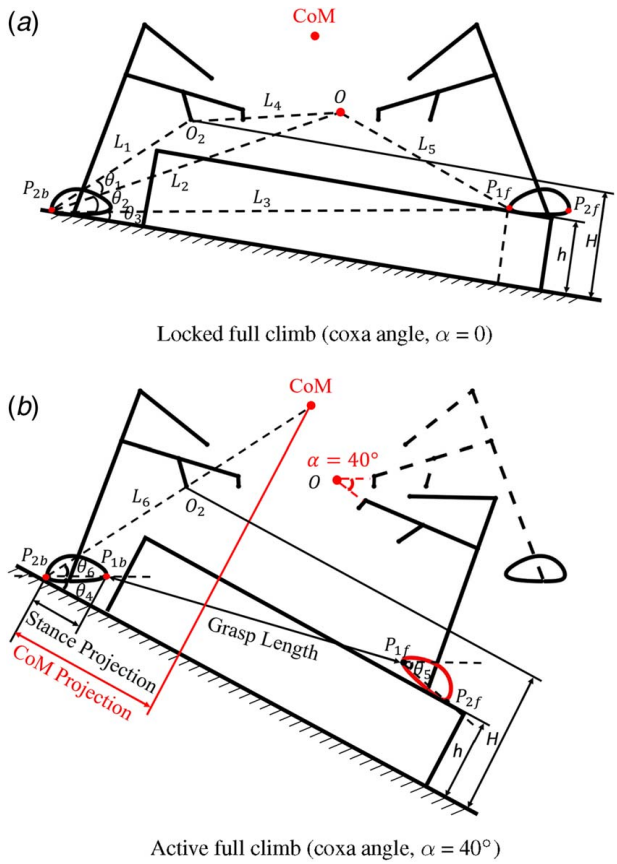

Fig. 5 The kinematics define the obstacle height, *h*, the robot can fully climb onto, with either locked (*a*) or active (*b*) coxa joint. The body height, *H*, is much higher with an active coxa, and the grasp length is adjustable. These diagrams are shown with horizontal ground rotated into a body reference frame defined in Fig. 4.

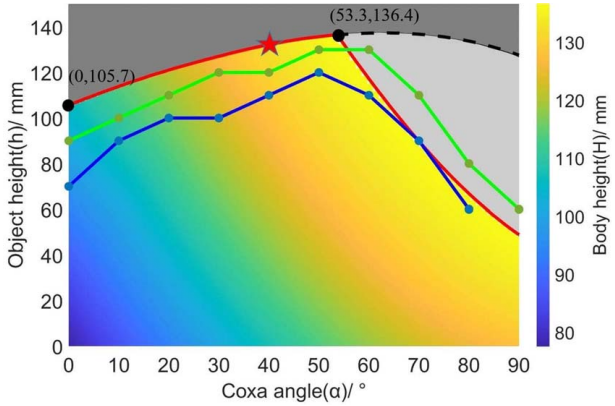

Fig. 6 Full climb analysis depicts the climbable workspace versus α and H considering both failure conditions, which are the deep gray area (which violates Eq. (4)) and the light gray area (which violates Eq. (5)). The red line shows the predicted maximum climbable obstacle height, where the maximum height is 136.4 mm at 53.3° (74% robot height). The star shows the kinematic prediction when $\alpha = 40°$ as Fig. 5(*b*). The green line is the simulation data. The blue line is the experimental result of the robot.

$$\begin{aligned} H &= L_1 * \sin(\theta_1 + \theta_2 + \theta_3) \\ &= L_1 * \sin(\theta_1 + f_1(\alpha) + f_2(\alpha, h)) \\ &= f_3(\alpha, h) \end{aligned} \tag{3}$$

Since P_1P_2 is the approximate stance phase, P_{2b} is considered as the point when the back legs touch the ground (P_{ib} refers to the P_i on the back gait. P_{if} refers to the P_i on the front gait, $i = 1$ or 2). However, for front legs, either P_{1f} or P_{2f} is possible to contact top of the object. If $\theta_4 < \theta_5$, P_{1f} will be the contact point (Fig. 5(*a*)), otherwise, P_{2f} will be (Fig. 5(*b*)). θ_4 is the angle between the ground and $P_{1b}P_{2b}$. θ_5 is the angle between the horizon and $P_{1f}P_{2f}$. To successfully clear the top of the object, the body height should be large than the obstacle height (Eq. (4)). Before $\theta_1 + \theta_2 + \theta_3$ reaches $\pi/2$, when α becomes larger, H is larger if h is fixed. However, it is not always true that a bigger coxa angle is preferred due to problems, such as unsuitable walking gait and unstable support polygon. Slowing down the motor speed can mitigate the vibration caused by bad gaits. To achieve static stability, the CoM must lie in the support polygon defined by the end effectors. Thus, the CoM projection should be larger than the stance projection (Eq. (5)), where L_6 is the distance between CoM and P_{2b}, θ_6 is the angle between L_6 and $P_{1b}P_{2b}$.

$$h < H \tag{4}$$

$$P_{1b}P_{2b} * \cos(\theta_4) < L_6 * \cos(\theta_4 + \theta_6)) \tag{5}$$

Body height (H) versus obstacle height (h) versus coxa angle (α) is shown in Fig. 6. It depicts the available workspace (colored area), while the red line is the maximum climbable height in every coxa angle from 0° to 90° CW. Though body height is limited by invariable L_1, the maximum active climbable height is 136.4 mm (76.6% robot height) when the best coxa angle is 53.3°. In contrast, the gray workspace shows the full climb failure. According to Eqs. (4) and (5), full climb failure above the dashed line (deep gray area) is a lack of body height, while failure below it (light gray area) is that CoM is out of support polygon. To prove the full climb analysis, in the following sections, Webots simulation, and physical experiments were conducted on adjustable stairs with different coxa angles. The green line was the simulation result. The blue line depicted the experimental results.

In general, the half climb mainly relies on the gait height so that the active prediction is 280 mm, whereas the locked prediction is only 14.8 mm. For the full climb, though the body height at 0° is 105.7 mm, the locked full climb is limited by a failed half climb. Thus the locked full climb prediction is the same as the locked half climb (14.8 mm). In contrast, with the coxa joint, the robot can reach 136.4 mm when raising the body by pressing the front legs down.

3.2.3 Grasp and Pull. Finally, grasping depends on the grasp length $P_{1f}P_{1b}$. The locked Klann robot has nearly no ability to grasp. Even if the robot climbs onto an obstacle that is exactly the grasp length max, and the legs drop down on either side, the robot has no ability to pull the legs inward since they are driven together. Even if the front and rear legs were driven separately, the maximum theoretical grasp range would be limited by the stride length (47.9 mm). However, the number of degrees-of-freedom even without the coxa would be four and the climbing height would not be increased.

The lift DOF also changes the grasp length, which enables the legs to press into the sides of the obstacle. Based on the grasp kinematics in Fig. 5(*b*), the maximum grasp length is 371 mm (89% robot length), and the minimum grasp length is 167 mm (40% robot length). Thus the range of object sizes that are graspable is 204 mm. The self-locking driving system on the coxa joint holds tightly without any input power due to the thread-locking of the worm drive system. After the robot grips tightly on the object, the tether can be pulled, and object retrieval is completed, as shown in Fig. 7. The coxa is driven by a high gear ratio DC motor (10:1, 4.9 kg · cm) and worm gearbox (40:1). Before raising the tether, vertical friction does not exist. The maximum normal force can be calculated as the following equation:

$$\begin{aligned} N &= M_{\text{coxa}}/OP_1 \\ &= 4.9 * 40/10.9 = 10\,\text{kg} \end{aligned} \tag{6}$$

The maximum moment arm of the normal force is no longer than OP1 (10.9 cm) so that the maximum horizontal normal force from one coxa is bigger than 18.0 kg.

4 Robot Assembly

4.1 Hardware Components. To avoid complexity in the control system and maintain sufficient power in continuous rotation, DC motors (Pololu 3203 (Drive DOF: gear ratio 20.4:1, 12 V, 500 rpm, 7.4 kg · cm) and Pololu 4748 (Lift DOF: gear ratio 10:1, 12 V, 1000 rpm, 4.9 kg · cm) are chosen because of their simplicity, high torque, and favorable size. Between the Pololu 3203 and dual Klann legs, drive-gearboxes (gear ratio 3:1) are used to produce enough torque to perform the periodic gait. With the Pololu 4748 paired with the coxa joints, worm-gearboxes are chosen as they are non-backdrivable and can achieve high gear reductions in a small space (gear ratio 40:1), allowing the robot to hold its stance or grip without further input power.

The robot is driven by two dual H-bridge pulse width modulation (PWM) motor drivers, powered by a 12 V power source. The robot operator is able to move the robot manually with a joystick controller (Flysky FS-I6X) via an RC transmitter and receiver (Flysky FS-IA6B). Arduino Mega 2560 receives the control signal from RC transmitter and receiver and then controls the voltage output of motor drivers. The joystick control interface is shown in Fig. 8. Since the robot is manually controlled and designed to work in disaster places, simplicity and stability are highly considered. Thus, no sensor feedback is included in the robotic system for both physical experiments and simulation. This work focuses on the mechanical structure of this kind of legged robot to position legs for grasping without additional manipulators. Sensors will be included in future work to help the robot develop an automatic searching and object retrieval control system.

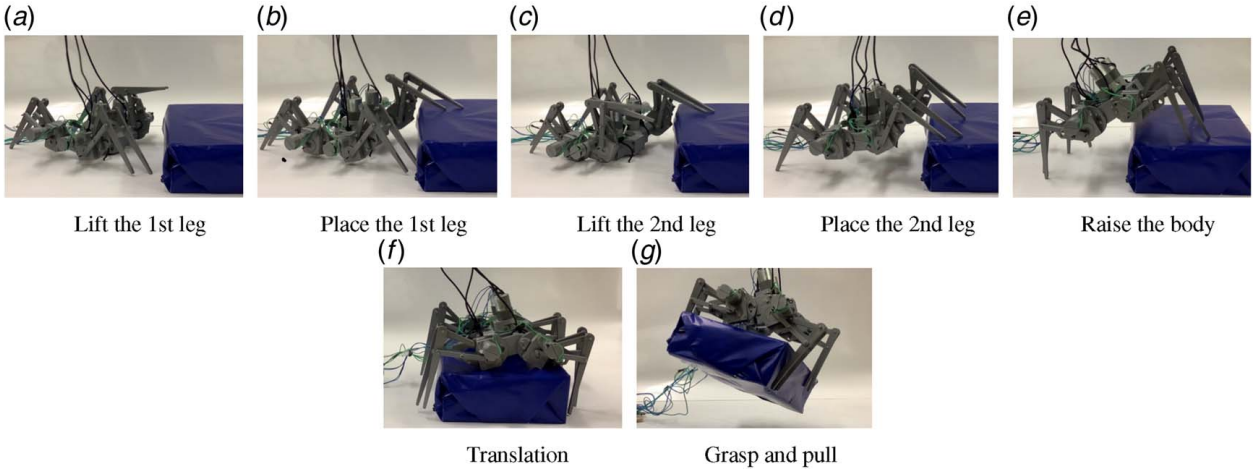

Fig. 7 Side view of object retrieval: (*a*) – (*d*) half climb, (*e*), (*f*) full climb, and (*g*) grasp and pull

Fig. 8 Joystick control strategy: The right stick controls the drive DOF, moving the robot in four different directions (forward, backward, left, and right). The left joystick controls the lift DOF, moving the target leg up or down. The vertical axis of the left stick is used to select which side's coxa is adjusted.

4.2 Fabrication. The main chassis, several of the gearboxes, and all links are 3D printed in polylactic acid (PLA). The leg gearbox utilizes brass gears and bushings. Nylon washers are placed between every fastener and every mating surface of the Klann linkage to reduce friction. The weight of four dual Klann legs is 1.12 kg; adding two coxa joints increases the total weight up to 2.03 kg (181% weight of four dual legs). Specifications of the articulated Klann robot and the length of Klann links are shown in Table 1.

5 Performance Simulation

To prove the kinematic predictions above, a Webots-based simulation was conducted to test the ability of the object retrieval. Environment parameters were set as follows: gravity coefficient 9.8 m/s^2, the material density of the robot 1250 kg/m^3 (PLA), the mass of Pololu 3203 (85 g), the mass of Pololu 4748 (175 g), the friction coefficient between the robot and ground 0.3 (friction coefficient between plastic and concrete), the friction coefficient between the robot and the obstacle 0.4 (friction coefficient between plastic and hardwood), the weight of the rectangular object 2 kg, and constraints of revolution joints. The friction coefficient can be found in Ref. [49]. All component models were input into Webots, then assembled together with six motors as drive DOF and lift DOF. Since Webots can't compute complex contact and constraint problems, if the motor speed is too fast, the simulation will have failed results. As a result, the drive motor speed was set as 2 rad/s in Webots, however, the motor speed was 11.3 rad/s when it walked on the lab tiles at 0° (walking speed is 0.173 m/s. One stride length is 47.9 mm. Each rotation period contains two stance phases). The lift motor speed was 0.5 rad/s to maintain balance while raising legs or pushing inward against the object. The simulation was manually preprogrammed. Thus, instead of automatical climbing and grasping with sensor feedback, the robot directly follows the position sequence in the controller code. The trail of experiments is three.

To evaluate the climbing performance, the robot was tested by half climbing onto an object, and then full climbing over it. The height of the artificial stair was adjustable ([5:1:20] cm) with a fixed width of 25 cm and a length of 50 cm. For the locked robot, it could only half climb 2 cm and then full climb 2 cm. A full climb was limited by a failed half climb. To test the active robot, the robot first needed to approach the object properly. Specifically, the front face of the object was 70° from the moving direction as Fig. 9. After moving the robot to its ideal starting point, the half-body climb began, which was divided into two parts: lifting and placing the first front dual leg, and then repeating this process

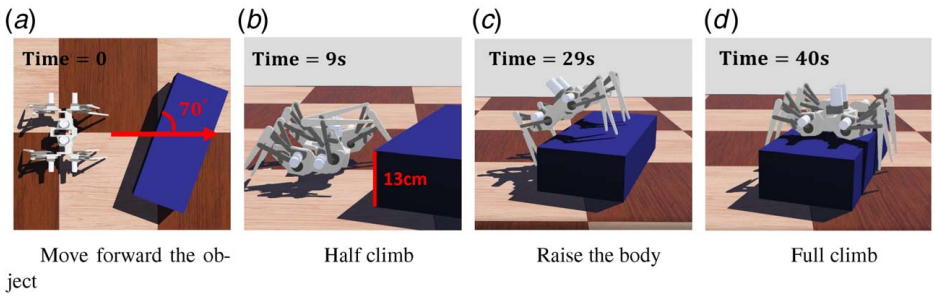

Fig. 9 Webots climb simulation: the robot successfully half climbed 20 cm and full climbed onto a 13 cm object: (*a*) move forward the object, (*b*) half climb, (*c*), raise the body, and (*d*) full climb

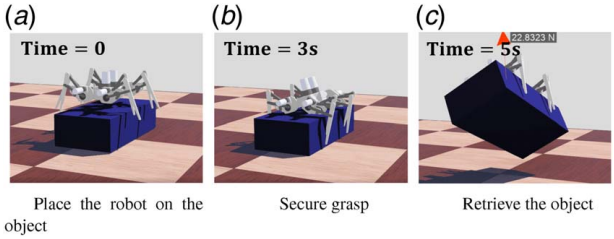

Fig. 10 Webots grasp simulation: the robot can grasp an object from 16 cm (38% robot length) to 29 cm (69% robot length). The available grasp range is 13 cm: (*a*) place the robot on the object, (*b*) secure grasp, and (*c*) retrieve the object

with the second front dual leg. According to kinematic analysis, α was set as 90° counterclockwise (CCW) to achieve the best half climb. Active full climb was tested at different coxa angles [0 : 10 : 90]°. In contrast to the locked result, the active robot could half climb up to 20 cm (112% robot height). The active half climb was only 71% prediction height, since a support polygon was not stable while lifting one front leg. The maximum active full climb was 13 cm (73% robot height) when α was 50° and 60°, shown in the green line in Fig. 6. Since the kinematic analysis only concerned Klann linkages, simulation results had a tradeoff to kinematics before 50° due to the additional chassis. However, it was better than predictions after 50° when CoM began to get close to the support polygon, since less vibration caused by low motor speed would mitigate problems with instability.

In the grasping test (Fig. 10), rectangles (fixed length 50 cm, fixed height 13 cm, width [15:1:38] cm) were set under the robot for further grasp. The trial of experiments is three. With the coxa angle manually controlled from 0 to 90° CW, the robot could securely retrieve the object from 16 cm (38% robot length) to 29 cm (69% robot length). The available grasp range was 13 cm. The minimum grasp length was close to the prediction (16.7 cm). However, the maximum length had some tradeoff to the kinematics (37.1 cm). The main reason for the deviation was that when rotating small coxa angle CW, it would be hard for the robot to maintain at least a parallel gripper. Thus, the friction was insufficient for a secure grasp. Changing the inner shape of end effectors or adding high friction material could solve this problem.

6 Experiments and Results

6.1 Evaluation of Speed. In the speed test, the robot was fully charged by the maximum voltage (12 V) to move forward on different flat terrains, such as lab tiles, carpet (polypropylene), a yoga mat (ethylene-vinyl acetate foam), and a bed of pebbles. The bed was 5 cm deep, full of pebbles with a diameter below 2 cm. Average speed was tested for 10 s for the lab tiles and carpet, 8 s for the yoga mat, and 6 s for pebbles because of the different sizes of testing environments. Three tests were completed on each terrain. To find how coxa joints affected the speed, the robot was tested with both coxa joints rotated to 15° CCW, 0° (locked), 15° CW, and 30° CW. More extreme coxa angles caused vibrations and low body chassis to contact the ground. The speed results are shown in Fig. 11.

The robot was the fastest overall on the smooth lab tiles. Then, the overall speeds on the yoga mat (ethylene-vinyl acetate foam) and carpet (polypropylene) were close, ranking second and third. Pebbles were the worst, since the legs can slide backward in the granular media. If only speed is considered, 30° CW is the best angle for lab tiles, 15° CW for carpet, 0° for both yoga mat and pebbles. In addition, 15° CCW was not good for all terrains due to low body height contacting the ground. Big coxa angles CW were also not ideal on the yoga mat and pebbles because the swing phase of the gait became more horizontal as the coxa angle CW became larger. This would cause the robot to be blocked by large pebbles or by foam when the leg sank a little into the yoga mat. As a result, a vertical swing phase with small coxa angles was more suitable for pebbles and yoga mats, such as 0° and 15° CW. However, 0° was not good for lab tiles and carpet. The robot would move faster due to bigger friction from dig motions around the touchdown point P_2, when rotating a bigger coxa angle CW (15° CW or 30° CW). Thus, the coxa is valuable in adjusting the robot for different terrains since there is no one position that is preferred for all terrains. The robot can walk on uneven terrains better with the preferred coxa angles of the specific terrain. In addition, stance height can be enlarged to walk across terrains with large obstacles by changing the Klann linkage [35].

In addition to the speed, the cost of transportation (COT) was 7.06 when the robot walked on the tiles at 0°, which indicated the energy efficiency of the Klann robot. It was close to the animals' equivalent data [50], though friction of rotational joints influenced the walking ability.

6.2 Evaluation of Climbing Performance. To evaluate the climbing performance, the robot was tested for first half climbing the adjustable package boxes, and then full climbing, like the simulation tests. Since we needed to customize boxes for testing, package boxes were used for both climbing and grasping. The top surface of the stair had enough friction for legs to step on without sliding. For the half climb at 90° CCW, the approach must be oblique to the front face of the object. When the first leg was placed onto the platform, the other front leg must have enough space to lift without hitting the object. For the full climb, coxa angles [0 : 10 : 90]° were tested. We tested the locked Klann robot and the active Klann robot three times for each obstacle

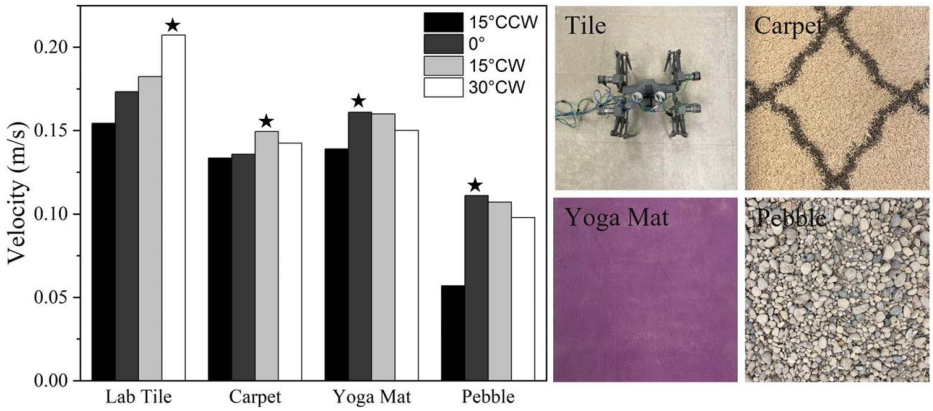

Fig. 11 Experimental results of speed on different terrains. A star indicates the maximum speed of each terrain

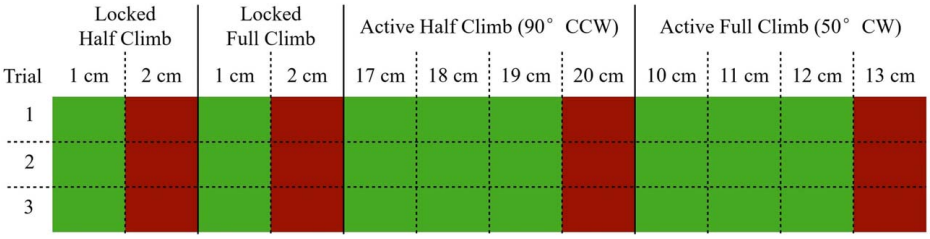

Fig. 12 Experimental climbing results: green is successful, red is failed. The active full climb only shows the result when α is 50°. Other experimental data with different coxa angles can be found in Fig. 6.

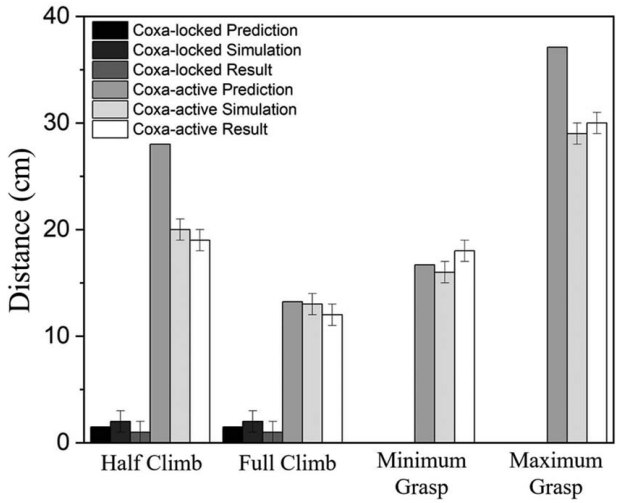

Fig. 13 Kinematic predictions, simulations, and results of half climb, full climb, and grasp. Error is 1 cm, the test resolution

height. Tests over 1 min are considered failures. The test video is uploaded to Youtube.[4]

Figure 12 shows the best experimental results on climbing performance. The locked robot succeeded in half climbing up to 10 mm. For higher obstacles, the end effector kicks the object without lifting the front legs up. In full climbing, the locked robot could climb up to 10 mm as well, which was limited by the locked gait height. This is lower than the simulation result of 2 cm, since PLA deformation would cause the gait shape inconsistent with the optimized gait in Fig. 2. Thus, lower the stance height. Overall, the active robot outperformed the locked robot in both half climb and full climb. The active half climb was up to 190 mm, though it was smaller than the prediction (280 mm) due to the same reason as the simulation (unstable support polygon). The first lifted dual leg would be closer to the ground than the kinematic analysis, thus resulting in some offset. Then, active full climb results with different coxa angles were shown in the blue line in Fig. 6. The active full climb was up to 120 mm at 50°, approximately to the prediction (136.4 mm). Though it was worse than the simulation due to vibrations caused by high-speed DC motors, the overall trend was close to simulation and the kinematic predictions. The kinematic prediction neglected chassis and PLA deformation, which would lower the actual climbing ability. Adjustments to chassis design and rigid material could mitigate this, but still, the predictions are reasonable.

6.3 Evaluation of Grasping. To evaluate the ability to grasp objects, the robot gripping was directly tested on different package boxes three times. Since we needed to customize boxes for testing, package boxes were used for grasping. From Sec. 3.2.3, the maximum ideal normal force is bigger than 18.0 kg. However, it would also damage the PLA leg and gearbox. Thus, the tested box weight was 2 kg, which didn't require such high normal force and was as heavy as the robot itself. Though the horizontal stride length was 47.9 mm, the locked robot was not capable of gripping because the front and back legs were not driven separately. Coxa joints enabled the robot to grasp objects with width from 180 mm (43% robot length) to 300 mm (72% robot length) by rotating coxa joints from 0° to 90°. This is comparable to the predicted grasp length from 167 mm to 371 mm. The minimum grasp length was close to the prediction. However, the maximum grasp was worse than predictions. Maximum grasp had the same problem with the simulation: small coxa angles didn't maintain a parallel gripper, thus upward force was insufficient. Kinematic predictions, simulation, and experimental results are shown in Fig. 13.

7 Conclusion and Discussion

In this paper, we presented the design and the development of a four DOF Klann robot with dual Klann legs and novel coxa joints. The robot can climb onto and grasp a range of objects for tethered retrieval and traverse various natural terrains. Unlike most mobile robots with additional manipulators, we combined the walking mechanism and the gripper so that the whole robotic platform was simple and stable. While the coxa mechanism and actuators may increase the weight of the robot by as much as 81%, the size of objects that can be full climbed is up to 12 cm. With the lift DOF, the robot would be able to securely grasp the object from 18 cm to 30 cm, making the lift DOF an important contribution for this type of robot. It is possible to grasp various shaped objects by changing the inner shape of the end effector and using high friction skin. In addition, we need to modify the robot to help it climb on different shapes, which will be included in future work. Climbing and grasping rectangular boxes are good to show the potential of this walking claw.

Overall, experimental results are close to simulation results. They both have a tradeoff to kinematic predictions of active half climb and the maximum grasp length. Unstable support polygon causes the active half climb lower than the predicted height, thus the next design will focus on the support problem. The maximum grasp length is influenced because the robot can't form at least a parallel gripper when the coxa angle is small. To improve the gripping ability, the inner shape of the end effector will be redesigned for better grasp shape and silicon will be used as high friction skin. Though simulations and tests are close to full climb prediction, adjustment to chassis design with rigid material will also improve full climb ability. Reversing the presented kinematics will enable future designers to construct simple walking claw robots to meet requirements for retrieving desired size objects.

In the future, the positioning for a grasp, which requires up to a minute with the current manual control, could be automated with dactyl sensors as we have previously used for terrain classification [45]. Once automated, teams of such robots could descend from a single spreader bar to coordinate automated lifts of large objects.

[4]https://www.youtube.com/watch?v=Dpry9H3EnSI

To establish form closure as well as force closure, the first lift could be small, just enough to pass rigging under the target object. Even more intelligent control could enable small crab-like robots to search an area for specific objects, and then send up buoys or quadcopters for collection when convenient.

Acknowledgment

The authors would like to thank the CWRU bio-robotics lab for their assistance throughout the project, especially Xiaoyue XU. This work was supported in part by the Office of Naval Research under a Young Investigator Award under Grant No. TTP19-0033 and in part by the Strategic Environmental Research and Development Program (SERDP) SEED under Grant No. MR19-1369. (Corresponding author: Kathryn Daltorio.)

Conflict of Interest

There are no conflicts of interest.

Data Availability Statement

The datasets generated and supporting the findings of this article are obtainable from the corresponding author upon reasonable request.

Nomenclature

h	=	obstacle height
H	=	body height in a full climb
O	=	coxa joint
r_1–r_7	=	seven Klann links
O_1–O_3	=	three fixed rotation joints of Klann linkage
P_1–P_6	=	gait definition points
CCW	=	counterclockwise
CoM	=	center of mass
CW	=	clockwise
DOF	=	degrees-of-freedom
α	=	coxa angle

References

[1] Hutter, M., Gehring, C., Jud, D., Lauber, A., Bellicoso, C. D., Tsounis, V., and Hwangbo, J., 2016, "Anymal - A Highly Mobile and Dynamic Quadrupedal Robot," IEEE/RSJ International Conference on Intelligent Robots and Systems (IROS), Daejeon, South Korea, October, pp. 38–44.

[2] Bjelonic, M., Kottege, N., Homberger, T., Borges, P., Beckerle, P., and Chli, M., 2018, "Weaver: Hexapod Robot for Autonomous Navigation on Unstructured Terrain," J. Field Rob., **35**(7), pp. 1063–1079.

[3] Raibert, M., Blankespoor, K., Nelson, G., and Playter, R., 2008, "Bigdog, the Rough-Terrain Quadruped Robot," IFAC Proc. Vol., **41**(2), pp. 10822–10825.

[4] Nelson, G., Saunders, A., and Playter, R., 2018, "The Petman and Atlas Robots At Boston Dynamics," Humanoid Rob.: A Reference, **169**, p. 186.

[5] Huang, K.-J., Chen, S.-C., Komsuoglu, H., Lopes, G., Clark, J., and Lin, P.-C., 2015, "Design and Performance Evaluation of a Bio-Inspired and Single-Motor-Driven Hexapod Robot With Dynamical Gaits," ASME J. Mech. Rob., **7**(3), p. 031017.

[6] Hussain, I., Renda, F., Iqbal, Z., Malvezzi, M., Salvietti, G., Seneviratne, L., Gan, D., and Prattichizzo, D., 2018, "Modeling and Prototyping of An Underactuated Gripper Exploiting Joint Compliance and Modularity," IEEE Rob. Autom. Lett., **3**(4), pp. 2854–2861.

[7] Zimmermann, S., Poranne, R., and Coros, S., 2021, "Go Fetch! - Dynamic Grasps Using Boston Dynamics Spot With External Robotic Arm," IEEE International Conference on Robotics and Automation (ICRA), Xi'an, China, May, pp. 4488–4494.

[8] Giftthaler, M., Farshidian, F., Sandy, T., Stadelmann, L., and Buchli, J., 2017, "Efficient Kinematic Planning for Mobile Manipulators With Non-Holonomic Constraints Using Optimal Control," 2017 IEEE International Conference on Robotics and Automation (ICRA), Singapore, May.

[9] Heins, A., Jakob, M., and Schoellig, A. P., 2021, "Mobile Manipulation in Unknown Environments With Differential Inverse Kinematics Control," Conference on Robots and Vision (CRV), Burnaby, BC, Canada, May, pp. 64–71.

[10] Murphy, R. R., 2017, *Disaster Robotics*, MIT Press, Cambridge, MA.

[11] Filardo, P., 2021, Pliant Energy Systems/NACROM – 2020 Underwater Minerals Conference

[12] Dong, W., Ding, Y., Yang, L., Sheng, X., and Zhu, X., 2019, "An Efficient Approach for Stability Analysis and Parameter Tuning in Delayed Feedback Control of a Flying Robot Carrying a Suspended Load," ASME J. Dyn. Syst. Meas. Contr., **141**(8), p. 081015.

[13] IEEE Spectrum, 2015, A Compilation of Robots Falling Down at the DARPA Robotics Challenge.

[14] Banerjee, N., Long, X., Du, R., Polido, F., Feng, S., Atkeson, C. G., Gennert, M., and Padir, T., 2015, "Human-Supervised Control of the Atlas Humanoid Robot for Traversing Doors," IEEE-RAS 15th International Conference on Humanoid Robots (Humanoids), Seoul, South Korea, November, pp. 722–729.

[15] Kang, P., Han, L., Xu, W., Wang, P., and Yang, G., 2019, "Mobile Robot Manipulation System With a Reconfigurable Robotic Arm: Design and Experiment," IEEE International Conference on Robotics and Biomimetics (ROBIO), Dali, China, December, pp. 2378–2383.

[16] Liu, J., Iacoponi, S., Laschi, C., Wen, L., and Calisti, M., 2020, "Underwater Mobile Manipulation: A Soft Arm on a Benthic Legged Robot," IEEE Rob. Autom. Mag., **27**(4), pp. 12–26.

[17] Yin, A., Lin, H.-C., Thelen, J., Mahner, B., and Ranzani, T., 2019, "Combining Locomotion and Grasping Functionalities in Soft Robots," Adv. Intell. Syst., **1**(8), p. 1900089.

[18] Venkiteswaran, V. K., Tan, D. K., and Misra, S., 2020, "Tandem Actuation of Legged Locomotion and Grasping Manipulation in Soft Robots Using Magnetic Fields," Extreme Mech. Lett., **41**, p. 101023.

[19] Rimon, E., and Burdick, J., 1996, "On Force and Form Closure for Multiple Finger Grasps," Proceedings of IEEE International Conference on Robotics and Automation, Minneapolis, MN, April, Vol. 2, pp. 1795–1800.

[20] Wile, G. D., Daltorio, K. A., Diller, E. D., Palmer, L. R., Gorb, S. N., Ritzmann, R. E., and Quinn, R. D., 2008, "Screenbot: Walking Inverted Using Distributed Inward Gripping," IEEE/RSJ International Conference on Intelligent Robots and Systems, Nice, France, September, pp. 1513–1518.

[21] Miller, T. G., Bretl, T. W., and Rock, S., 2006, "Control of a Climbing Robot Using Real-Time Convex Optimization," IFAC Proc. Vol., **39**(16), pp. 409–414.

[22] Graf, N. M., Behr, A. M., and Daltorio, K. A., 2021, "Dactyls and Inward Gripping Stance for Amphibious Crab-Like Robots on Sand," Bioinspir. Biomim., **16**(2), p. 026021.

[23] Yuan, S., Epps, A. D., Nowak, J. B., and Salisbury, J. K., 2020, "Design of a Roller-Based Dexterous Hand for Object Grasping and Within-Hand Manipulation," IEEE International Conference on Robotics and Automation (ICRA), Paris, France, May.

[24] Wei, Y., Chen, Y., Ren, T., Chen, Q., Yan, C., Yang, Y., and Li, Y., 2016, "A Novel, Variable Stiffness Robotic Gripper Based on Integrated Soft Actuating and Particle Jamming," Soft Rob., **3**(3), pp. 134–143.

[25] Feix, T., Romero, J., Schmiedmayer, H.-B., Dollar, A. M., and Kragic, D., 2016, "The Grasp Taxonomy of Human Grasp Types," IEEE Trans. Human-Mach. Syst., **46**(1), pp. 66–77.

[26] Wattanasiri, P., Tangpornprasert, P., and Virulsri, C., 2018, "Design of Multi-Grip Patterns Prosthetic Hand With Single Actuator," IEEE. Trans. Neural. Syst. Rehabil. Eng., **23**(6), pp. 1188–1198.

[27] Tawk, C., Gillett, A., Spinks, G. M., and Alici, G., 2019, "A 3D-Printed Omni-Purpose Soft Gripper," IEEE Trans. Rob., **35**(5), pp. 1268–1275.

[28] Xiong, Y., Peng, C., Grimstad, L., From, P. J., and Isler, V., 2019, "Development and Field Evaluation of a Strawberry Harvesting Robot With a Cable-Driven Gripper," Comput. Electron. Agricul., **157**, pp. 392–402.

[29] Allen, T., Quinn, R., Bachmann, R., and Ritzmann, R., 2003, "Abstracted Biological Principles Applied With Reduced Actuation Improve Mobility of Legged Vehicles," Proceedings 2003 IEEE/RSJ International Conference on Intelligent Robots and Systems (IROS 2003), Las Vegas, NV, October, Vol. 2, pp. 1370–1375.

[30] Campbell, D., and Buehler, M., 2003, "Stair Descent in the Simple Hexapod 'RHex'," 2003 IEEE International Conference on Robotics and Automation , Taipei, Taiwan, September, Vol. 1, pp. 1380–1385.

[31] Wei, T., Quinn, R., and Ritzmann, R., 2005, "Robot Designed for Walking and Climbing Based on Abstracted Cockroach Locomotion Mechanisms," Proceedings, 2005 IEEE/ASME International Conference on Advanced Intelligent Mechatronics., Monterey, CA, July, pp. 1471–1476.

[32] theo jansenl, 2021, Strandbeest Evolution 2020.

[33] Yul Shin, S., Deshpande, A. D., and Sulzer, J., 2018, "Design of a Single Degree-of-Freedom, Adaptable Electromechanical Gait Trainer for People With Neurological Injury," ASME J. Mech. Rob., **10**(4), p. 044503.

[34] Fedorov, D., and Birglen, L., 2017, "Design of a Self-Adaptive Robotic Leg Using a Triggered Compliant Element," IEEE Rob. Autom. Lett., **2**(3), pp. 1444–1451.

[35] Sheba, J. K., Martínez-García, E., Elara, M. R., and Tan-Phuc, L., 2015, "Design and Evaluation of Reconfigurable Klann Mechanism Based Four Legged Walking Robot," 2015 10th International Conference on Information, Communications and Signal Processing (ICICS), Singapore, December, pp. 1–5.

[36] Kulandaidaasan Sheba, J., Elara, M. R., Martínez-García, E., and Tan-Phuc, L., 2016, "Trajectory Generation and Stability Analysis for Reconfigurable Klann Mechanism Based Walking Robot," Robotics, **5**(3), p. 13.

[37] Kim, H.-G., Jung, M.-S., Shin, J.-K., and Seo, T., 2014, "Optimal Design of Klann-Linkage Based Walking Mechanism for Amphibious Locomotion on Water and Ground," J. Inst. Control, Rob. Syst., **20**(9), pp. 936–941.

[38] Kavlak, K., and Kartal, I. A., 2021, "Kinematic Analysis of Mobile Robot With Klann Walking Mechanism," 2021 3rd International Congress on Human-Computer Interaction, Optimization and Robotic Applications (HORA), Ankara, Turkey, June, pp. 1–6.

[39] Kamimura, T., Aoi, S., Tsuchiya, K., and Matsuno, F., 2018, "Body Flexibility Effects on Foot Loading in Quadruped Bounding Based on a Simple Analytical Model," IEEE Rob. Autom. Lett., **3**(4), pp. 2830–2837.
[40] Seo, T., and Sitti, M., 2013, "Tank-Like Module-Based Climbing Robot Using Passive Compliant Joints," IEEE/ASME Trans. Mechatron., **18**(1), pp. 397–408.
[41] Boxerbaum, A. S., Oro, J., Peterson, G., and Quinn, R. D., 2008, "The Latest Generation Whegscha™ Robot Features a Passive-Compliant Body Joint," 2008 IEEE/RSJ International Conference on Intelligent Robots and Systems, Nice, France, September, pp. 1636–1641.
[42] Wile, G. D., Daltorio, K. A., Palmer, L. R., Witushynsky, T. C., Southard, L., Ahmad, M. R., and Malek, A. A., 2008, "Making Orthogonal Transitions With Climbing Mini-Whegs™," 2008 IEEE International Conference on Robotics and Automation, Pasadena, CA, May, pp. 1775–1776.
[43] Wei, T., Quinn, R., and Ritzmann, R., 2005, "A Clawar That Benefits From Abstracted Cockroach Locomotion Principles," Climbing and Walking Robots, Berlin/Heidelberg.
[44] Bledt, G., Powell, M. J., Katz, B., Di Carlo, J., Wensing, P. M., and Kim, S., 2018, "Mit Cheetah 3: Design and Control of a Robust, Dynamic Quadruped Robot," 2018 IEEE/RSJ International Conference on Intelligent Robots and Systems (IROS), Madrid, Spain, October, pp. 2245–2252.
[45] Grezmak, J., Graf, N., Behr, A., and Daltorio, K., 2021, "Terrain Classification Based on Sensed Leg Compliance for Amphibious Crab Robot," IEEE Sensors J., **21**(20), pp. 23308–23316.
[46] Wu, J., Yang, H., Li, R., Ruan, Q., and Yan, S., 2021, "Design and Analysis of a Novel Octopod Platform With a Reconfigurable Trunk," Mech. Mach. Theory., **156**, p. 104134.
[47] Wu, J., Yao, Y.-a., Li, Y., Wang, S., and Ruan, Q., 2019, "Design and Analysis of a Sixteen-Legged Vehicle With Reconfigurable Close-Chain Leg Mechanisms," ASME J. Mech. Rob., **11**(5), p. 055001.
[48] Daltorio, K. A., Witushynsky, T. C., Wile, G. D., Palmer, L. R., Ab Malek, A., Ahmad, M. R., Southard, L., Gorb, S. N., Ritzmann, R. E., and Quinn, R. D., 2008, "A Body Joint Improves Vertical to Horizontal Transitions of A Wall-Climbing Robot," 2008 IEEE International Conference on Robotics and Automation, Pasadena, CA, May, pp. 3046–3051.
[49] Friction Coefficients Between Different Wheel/Tire Materials and Concrete https://mae.ufl.edu/designlab/Class%20Projects/Background%20Information/Friction%20coefficients.htm.
[50] Kim, S., and Wensing, P. M., 2017, "Design of Dynamic Legged Robots," Found. Trends Rob., **5**(2), pp. 117–190.